arXiv:2512.24303v3 [cond-mat.soft] 15 Apr 2026

Mixing, segregation, and collapse transitions of interacting copolymer rings

E J Janse van Rensburg[1], E Orlandini[2], M C Tesi[3] and S G Whittington[4]
[1] Department of Mathematics and Statistics, York University, Toronto, Ontario M3J 1P3, Canada
[2] Dipartimento di Fisica e Astronomia e Sezione INFN, Università di Padova, Via Marzolo 8, I-35131 Padova, Italy
[3] Dipartimento di Matematica, Università di Bologna, Piazza di Porta San Donato 5, I-40126 Bologna, Italy
[4] Department of Chemistry, University of Toronto, Toronto M5S 3H6, Canada

April 17, 2026

Abstract

A system of two self and mutual interacting ring polymers, close together in space, can display several competing equilibrium phases and phase transitions. Using Monte Carlo simulations and combinatorial arguments on a corresponding lattice model, we determine three equilibrium phases, two in which the rings segregate in space and are either extended (the segregated-expanded phase) or compact (the segregated-collapsed phase). The third is a mixed phase where the rings interpenetrate. The corresponding phase boundaries are located numerically and their critical nature is discussed. Finally, by looking at the topological properties of the three phases, we show that the two rings are likely to be linked in the mixed phase and knotted in the segregated-collapsed phase.

Keywords: Links, lattice polygons, polymer collapse, Monte Carlo methods.

1 Introduction

In this paper we investigate a model of two ring polymers that are required to be close together in space. The monomers in the two rings are different and this can lead to a mixed phase where the two rings interpenetrate [1]. In addition, either or both of the rings can collapse to form a compact ball. This model is connected to the behaviour of a diblock copolymer.

The synthesis of catenated ring polymers [2, 3], often in AB-diblock form [4] with one ring the A-block and the other ring the B-block, presents a novel situation with a phase diagram admitting several possible phases, including segregated, collapsed and mixed phases in a dilute solution, in addition to additional phases when the diblock catenane is in a melt or in confinement [3]. The linking of components in a catenane mix results in interlocking ring polymer sheets [5] resembling chainmail and held together by mechanically bonded rings due to the physical linking of the component ring polymers. Numerical simulations of catenated ring copolymers show that the rings are pulled together by catenation, giving rise to smaller radii of gyration (when compared to a

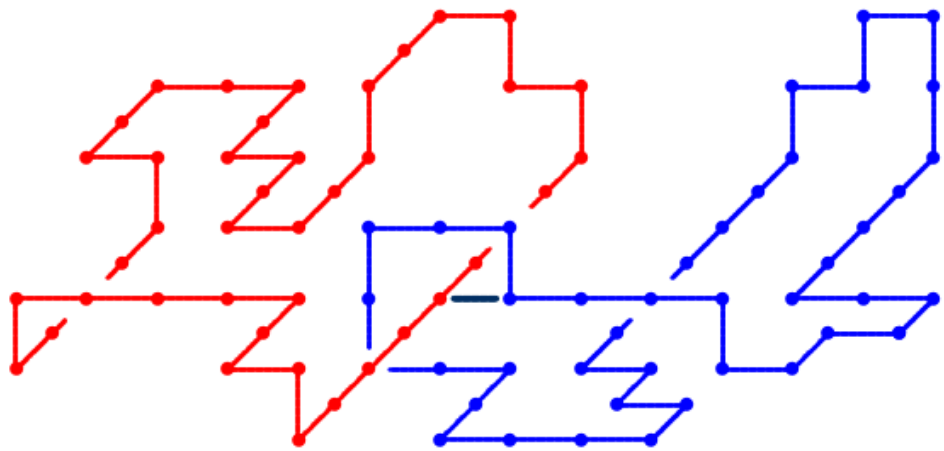

Figure 1: A cubic lattice model of an AB-diblock catenane with an A-block (red) and a B-block (blue). We implement this model by sampling lattice polygons while keeping the two polygons near each other. This is done by having at least one vertex in the A-block a unit distance from a vertex in the B-block. A pair of such vertices are marked with the solid line in the figure. The two polygons can be linked (as in this figure) to model a catenane.

single ring of the same length) and reduced distance between the centres of mass [6, 1]. Furthermore, it has been shown that ring-shaped polycatenanes have the capacity to retain a relevant quantity of twist, which significantly alters their metric and local properties [7].

A cubic lattice model of two ring copolymers in a dilute solution that may be catenated consists of two interacting ring polymers (namely, lattice polygons) as illustrated in figure 1. The two polygons are held in proximity, and we examine metric and linking properties using Monte Carlo simulations. This approach is broadly similar to the study in reference [6], but with additional (repulsive or attractive) short-ranged forces between monomers in the two respective component polygons, which are also (independently) self-interacting if there are forces between monomers in each. This distinguishes the two polygons, so that, when catenated, they are a model of an AB-diblock ring polymer, with one ring the A-block and the other ring the B-block.

If the self-interacting forces between monomers in each component polygon are large, then they go through θ-points to collapsed regimes, while, if the forces between monomers in each block (one in the A-block, and the other in the B-block) are large, then the two component polygons should interpenetrate each other, moving into a mixed regime. If either of the A- or B-blocks are collapsed, then they are in a collapsed or globular phase with increased self-entanglements as observed by the increased probability that they are non-trivial knots [8]. In the mixed regime the probability that the components form a catenane is increased [9, 10, 1]. We investigate this by examining the linking probability of the A- and B-blocks as a function of the interaction between the components.

We implement the model in figure 1 by considering two lattice polygons (or closed self-avoiding walks) of the same length on the simple cubic lattice. The two polygons are held together in the lattice by having at least one vertex in one polygon (this is the A-block) a unit distance from a vertex in the other polygon (namely the B-block). There are three energy terms in this model. If

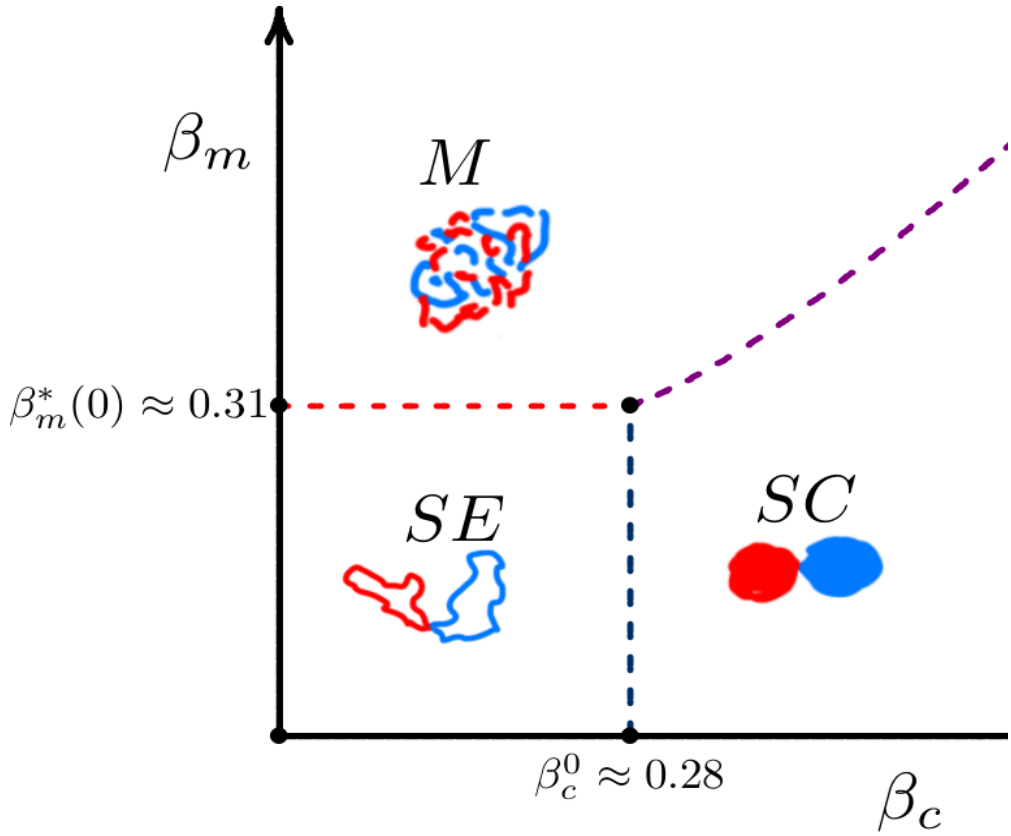

Figure 2: A hypothetical sketch of the model's expected phase diagram. There are at least three possible phases of mixed(M) or expanded(E)-collapsed(C) copolymer. The segregated-expanded (SE), segregated-collapsed (SC) and mixed (M) phases are explored in this paper.

two monomers of type A are unit distance apart and not connected by an edge of the polygon, then they form an AA-*contact* and they contribute an energy ϵ_{AA} to the total energy of the system. Similarly, two monomers of type B a unit distance apart form a BB-contact and contribute an energy ϵ_{BB}, and a pair of monomers of types A and B a unit distance apart form an AB-contact and contribute an energy ϵ_{AB}. If $\epsilon_{AA} < 0$ this will favour collapse of the A-ring into a globular phase, and similarly, $\epsilon_{BB} < 0$ will favour collapse of the B-ring. If $\epsilon_{AB} < 0$, this will favour intermingling of the two polygons and a transition to a mixed phase where we examine the linking probability of the two rings [1].

If we set $\epsilon_{AA} = \epsilon_{BB}$, then both rings will collapse at the same temperature. In that case we expect at least three phases: A segregated-expanded phase where the rings are largely separated in space and each is expanded as in a good solvent, a segregated-collapsed phase where the two rings are largely separated but each ring has collapsed to a compact ball, and a mixed phase where the two rings interpenetrate to a significant extent. The phase diagram is illustrated in figure 2. We expect three phase boundaries in the phase diagram. The phase transition between the segregated-expanded and segregated-collapsed phases when $\epsilon_{AB} = 0$ is relatively well understood. It is the collapse transition for a ring polymer.

The transition from the segregated-expanded phase to the mixed phase was investigated in [1]

but the transition from the segregated-collapsed phase to the mixed phase has not previously been investigated. If we write $\beta_m = -\epsilon_{AB}/kT$ and $\beta_c = -\epsilon_{AA}/kT = -\epsilon_{BB}/kT$, where k is Boltzmann's constant and T is the absolute temperature, then we can look at the (β_c, β_m) plane and the phase boundaries will be lines or curves in this plane.

We use several techniques to investigate this phase diagram. In section 3, we use rigorous arguments to establish the existence of a phase boundary as β_m is increased, for all $\beta_c < \infty$. We write this phase boundary as $\beta_m^*(\beta_c)$ in the phase diagram. Note that $\beta_m^*(\beta_c)$ is a function of β_c and is the phase boundary separating the mixed M-phase from the segregated SE- and SC-phases (see figure 2). Similarly, we denote a phase boundary seperating the expanded SE-phase and the mixed M-phase from the collapsed SC-phase by $\beta_c^*(\beta_m)$.

If $\beta_c = 0$ then the model has a transition from the SE-phase to the M-phase at the critical point $\beta_m^*(0)$, where we understand that $\beta_m^*(0)$ is the critical point for the transition when $\beta_c = 0$. We similarly define the critical point β_c^0 separating the SE- and SC-phases when $\beta_m = 0$. It is thought that the transition at β_c^0 is second order and there are good numerical estimates of its location [11, 12]. The estimates are

$$\beta_c^0 = \begin{cases} 0.2782 \pm 0.0070, & \text{for collapsing polygons;} \\ 0.2779 \pm 0.0041, & \text{for collapsing walks.} \end{cases} \tag{1}$$

Our rigorous results leave many questions unanswered and we use Monte Carlo methods to obtain additional information. There are several quantities that one can examine to probe the details of the phase diagram. These include thermodynamic quantities such as the energy and heat capacity, and metric properties such as the radii of gyration of the rings (to detect collapse), and the mean distance between the centres of gravity of the rings (to detect mixing). In addition, we can probe the extent of intermingling or mutual entanglement by calculating the linking probability of the two rings. We proceed by sampling and collecting data on the model along lines crossing the phase boundaries in the phase diagram, using a multiple Markov Chain implementation [13, 14] of the Metropolis algorithm [15] using Verdier-Stockmayer [16] and pivot [17] elementary moves which can change the knot type of lattice polygons and linking complexity between lattice polygons.

The plan of the paper is as follows: In section 2 we give a more detailed description of the lattice model that we use. Section 3 gives some rigorous results about the existence of a phase boundary between the mixed phase and the two segregated phases, and results about the shape of the phase boundary between the two segregated phases. We describe the Monte Carlo method that we use in section 4 and report our Monte Carlo results about the thermodynamic properties and metric properties in section 5 and about the topological properties in section 6. We close with a short discussion in section 7.

2 The model

The pair of self-avoiding lattice polygons has total length $2n$, and each has length n, both embedded in the cubic lattice, $\mathcal{Z}^3$. The polygons are also mutually avoiding and each has a root vertex placed such that the two roots are one lattice unit distance apart. We label the two polygons A and B and this setup can either describe two polymer rings linked together by a single chemical bond or a diblock copolymer with a figure eight connectivity.

Mutual interactions between the two polygons are *mutual contacts* (pairs of vertices $(v_A \in A, v_B \in B)$ such that the distance between v_A and v_B is one lattice unit). As above, there is

an interaction energy ϵ_{AB} for each mutual contact, and the total interaction energy from mutual contacts when a given configuration has k_m mutual contacts is $E_m = \epsilon_{AB} k_m$. In addition, each block is also subject to an effective self-attraction due to the quality of the solvent. By defining a *contact* within block A as a pair of non-consecutive vertices that are a unit distance apart, we have $E_A = \epsilon_{AA} k_A$ where $\epsilon_{AA} < 0$ is an effective attractive energy associated with each contact within block A and k_A is the number of such contacts. Similarly, for block B we have $E_B = \epsilon_{BB} k_B$ with $\epsilon_{BB} < 0$.

Define the parameters $\beta_m = -\epsilon_{AB}/kT$, $\beta_A = -\epsilon_{AA}/kT$ and $\beta_B = -\epsilon_{BB}/kT$ where k is Boltzmann's constant and T the absolute temperature. Then the partition function of the system is

$$Z_{2n}(\beta_m, \beta_A, \beta_B) = \sum_{k_m, k_A, k_B} p_{2n}^{(2)}(k_m, k_A, k_B)\, e^{\beta_m k_m + \beta_A k_A + \beta_B k_B}. \tag{2}$$

In equation (2) the function $p_{2n}^{(2)}(k_m, k_A, k_B)$ denotes the number of configurations of the two chemically distinct polygons with total length $2n$ having k_m mutual contacts, and k_A, k_B (self-)contacts within blocks A and B respectively. This general form accounts for the possibility of the two blocks having different affinities with the solvent. If we restrict to the simpler case of $\epsilon_{AA} = \epsilon_{BB} = \epsilon_c$ and define k_c to be the total number of contacts, i.e. $k_c = k_A + k_B$, then the partition function 2 simplifies to

$$Z_{2n}(\beta_m, \beta_c) = \sum_{k_m, k_c} p_{2n}^{(2)}(k_m, k_c)\, e^{\beta_m k_m + \beta_c k_c}, \tag{3}$$

where $\beta_c = -\epsilon_c/kT$. When $\beta_m < 0$ and $\beta_c < 0$ entropy should dominate and we do not expect a significant difference from the case with $\beta_m = 0$, $\beta_c = 0$. Thus, we restrict most of the analysis of the equilibrium phase diagram of the system to the values $\beta_m \geq 0$ and $\beta_c \geq 0$. In this range, mutual and self-attraction compete to determine the conformational properties of the system.

2.1 Preliminary considerations

We expect at least three equilibrium phases in the model, determined by the strength of the self-attraction ϵ_c, relative to the mutual attraction ϵ_m:

(i) For β_m and β_c sufficiently small the system should be in the *Segregated/Extended* (SE) phase, where the two rings are well separated in space and the average number of mutual contacts scaled by the systems size, $\langle k_m \rangle / 2n$, should approach zero in the thermodynamic limit ($n \to \infty$). Moreover, each polygon in the extended phase should display the metric properties of a self-avoiding polygon. Note that, by the pattern theorem [18], the self-contacts' density is non-zero, although small, in the thermodynamic limit. Concerning the topological properties, we expect a negligible amount of mutual (i.e. linking probability and link complexity) and self-topological entanglement (i.e. knotting probability and knot complexity) for the range of ring's lengths considered here ($n \in [48 - 400]$).

(ii) For $\beta_c \gg \beta_m$ and β_m still small the diblock copolymer rings should be in the *Segregated/Compact* (SC) phase where the two rings are still well separated in space ($\langle k_m \rangle / 2n \to 0$, as $n \to \infty$) but each ring displays a globular conformation (with metric properties of a compact phase). Consequently, the topological self-entanglement should increase dramatically while the mutual entanglements (measured by linking of the components) should remain negligible.

(iii) Above a critical value $\beta_m^*(\beta_c)$, the system is expected to be in a *Mixed* (M) phase where the two rings are significantly intermingled (the density of mutual contacts $\langle k_m \rangle / 2n$ is now positive in the thermodynamic limit). The *SE-M* transition occurs at the critical point $\beta_m^*(0) \approx 0.31$ for $\beta_c = 0$ [1] but, for $\beta_c \neq 0$, we expect $\beta_m^*(\beta_c)$ to be an increasing function of β_c for large β_c.

Finally we note that, to some extent, there is a similarity with the adsorption and collapse transition problem [19, 20]. In particular, the fact that the density of mutual contacts is negligible below the mixing transition could suggest that some features of the boundaries between the phases are similar. For instance, we might guess that the phase boundary between the SE and the SC phases (θ-point) does not depend on the value of β_m when $\beta_m < \beta_m^*(0)$.

A sketch of the possible phase diagram, which we shall study numerically, is given in figure 2. Monte Carlo simulations to carry out this investigation involve sampling at several points of the diagram sketched in figure 2, including large positive values of β_c and β_m.

3 Some rigorous results

Let $p_n(k_c)$ be the number of lattice polygons of length n steps in the cubic lattice with k_c nearest neighbour contacts between vertices. This defines a model of lattice polygons with nearest-neighbour self-interactions and partition function

$$P_n(\beta_c) = \sum_{k_c} p_n(k_c)\, e^{\beta_c k_c}.$$

It is known that the thermodynamic limit

$$\lim_{n\to\infty} \frac{1}{n} \log P_n(\beta_c) = \kappa_3(\beta_c) \tag{4}$$

exists in the cubic lattice for all $\beta_c < \infty$. More generally, this limit also exists in the hypercubic lattice [12], in which case the thermodynamic limit is denoted $\kappa_d(\beta_c)$. In the square lattice, it is denoted $\kappa_2(\beta_c)$. Clearly, $\kappa_2(\beta_c) \leq \kappa_3(\beta_c)$.

A dumbbell with a joining edge of length one is formed by placing two mutually disjoint lattice polygons and joining them with a single edge between a vertex in the first and a vertex in the second. If the number of such dumbbells with both polygons of length n, and a total of k_c nearest neighbour contacts within each polygon, and k_m nearest neighbour mutual contacts between the pair of polygons, is $p_{2n}^{(2)}(k_m, k_c)$, then the partition function is

$$Z_{2n}(\beta_m, \beta_c) = \sum_{k_m, k_c} p_{2n}^{(2)}(k_m, k_c)\, e^{\beta_m k_m + \beta_c k_c}$$

Theorem 1. *There exists a critical value $\beta_m^* \geq 0$ (a function of β_c) such that the limit*

$$\lim_{n\to\infty} \frac{1}{2n} \log Z_{2n}(\beta_m, \beta_c) = \phi(\beta_m, \beta_c)$$

exists for all $\beta_m < \beta_m^*(\beta_c)$ for all $\beta_c < \infty$.

Moreover, $\phi(\beta_m, \beta_c) = \kappa_3(\beta_c)$ if $\beta_m \leq \beta_m^*(\beta_c)$ and $0 \leq \beta_m^*(\beta_c) \leq 2\,\kappa_3(\beta_c) - \kappa_2(\beta_c)$.

Proof: A lattice polygon has a lexicographically least vertex (called the bottom vertex), and a lexicographically most vertex (called the top vertex). Two polygons can be placed and joined into a dumbbell if the bottom vertex of the second is one step in the x-direction above the top vertex of the first. These conformations correspond to terms with $k_m = 0$ in the partition function. Since the partition function of each polygon in the dumbbell is $P_n(\beta_c)$, this shows that

$$P_n^2(\beta_c) \leq Z_{2n}(\beta_m, \beta_c)$$

for all $\beta_m < \infty$ and $\beta_c < \infty$. By equation 4,

$$\kappa_3(\beta_c) \leq \liminf_{n\to\infty} \frac{1}{2n} \log Z_{2n}(\beta_m, \beta_c)$$

for all $\beta_m < \infty$ and $\beta_c < \infty$.

To obtain an upper bound we construct a box of side-length $2n$ and centre within one step from the centre-of-mass of the first polygon. Consider all placements of the second polygon with its centre-of-mass within this box. This gives the bound

$$(2n)^3\, P_n^2(\beta_c) \geq Z_{2n}(\beta_m, \beta_c), \quad \text{for all } \beta_m \leq 0 \text{ and } \beta_c < \infty.$$

This shows that

$$\kappa_3(\beta_c) \geq \limsup_{n\to\infty} \frac{1}{2n} \log Z_{2n}(\beta_m, \beta_c)$$

for all $\beta_m \leq 0$ and $\beta_c < \infty$. This shows that the limit

$$\lim_{n\to\infty} \frac{1}{2n} \log Z_{2n}(\beta_m, \beta_c) = \phi(\beta_m, \beta_c)$$

exists for all $\beta_m \leq 0$ and $\beta_c < \infty$ and is equal to $\kappa_3(\beta_c)$, and therefore independent of β_m, when $\beta_m \leq 0$.

We next consider the case that $\beta_m \geq 0$. Define $q_n(k_c)$ to be the number of polygons in the square lattice, of length n and with k_c nearest neighbour contacts. The partition function of this model is

$$Q_n(\beta_c) = \sum_{k_c} q_n(k_c)\, e^{\beta_c k_c}$$

and the free energy is given by

$$\kappa_2(\beta_c) = \lim_{n\to\infty} \frac{1}{n} \log Q_n(\beta_c)$$

and the limit exists for all $\beta_c < \infty$ [21].

Proceed by placing a square lattice polygon of length n with k_c contacts in the $z = 0$ plane, and an exact copy of it, translated one step in the z-direction in the $z = 1$ plane. Join these into a dumbbell by placing an edge between their bottom vertices. The number of mutual contacts is now $n-1$. This shows that

$$q_n(k_c) \leq p_{2n}^{(2)}(n-1, 2k_c)$$

Multiplying this by $e^{\beta_m(k-1)+2\beta_c k_c}$ and summing over k_c gives

$$\begin{aligned}\sum_{k_c} q_n(k_c)\, e^{\beta_m(n-1)+2\beta_c k_c} &\leq \sum_{k_c} p_{2n}^{(2)}(n-1, 2k_c)\, e^{\beta_m(n-1)+2\beta_c k_c} \\ &\leq \sum_{k_m, k_c} p_{2n}^{(2)}(k_m, 2k_c)\, e^{\beta_m k_m + 2\beta_c k_c}\end{aligned}$$

Replace β_c by $\beta_c/2$, take logarithms, divide by $2n$ and let $n \to \infty$ to see that

$$(\kappa_2(\beta_c) + \beta_m)/2 \leq \liminf_{n\to\infty} \frac{1}{2n} \log Z_{2n}(\beta_m, \beta_c)$$

for all $\beta_m < \infty$ and $\beta_c < \infty$.

If $\beta_m > 2\kappa_3(\beta_c) - \kappa_2(\beta_c) > 0$ then $(\kappa_2(\beta_c) + \beta_m)/2 > \kappa_3(\beta_c)$ showing that

$$\liminf_{n\to\infty} \frac{1}{2n} \log Z_{2n}(\beta_m, \beta_c) > \kappa_3(\beta_c).$$

Thus, there is a $\beta_m^*(\beta_c) \geq 0$ such that

$$\begin{aligned} \lim_{n\to\infty} \frac{1}{2n} \log Z_{2n}(\beta_m, \beta_c) &= \kappa_3(\beta_c), \quad \text{if } \beta_m \leq \beta_m^*(\beta_c) \text{ and} \\ \liminf_{n\to\infty} \frac{1}{2n} \log Z_{2n}(\beta_m, \beta_c) &> \kappa_3(\beta_c), \quad \text{if } \beta_m > \beta_m^*(\beta_c). \end{aligned}$$

Moreover, $0 \leq \beta_m^*(\beta_c) \leq 2\,\kappa_3(\beta_c) - \kappa_2(\beta_c)$.

This completes the proof. □

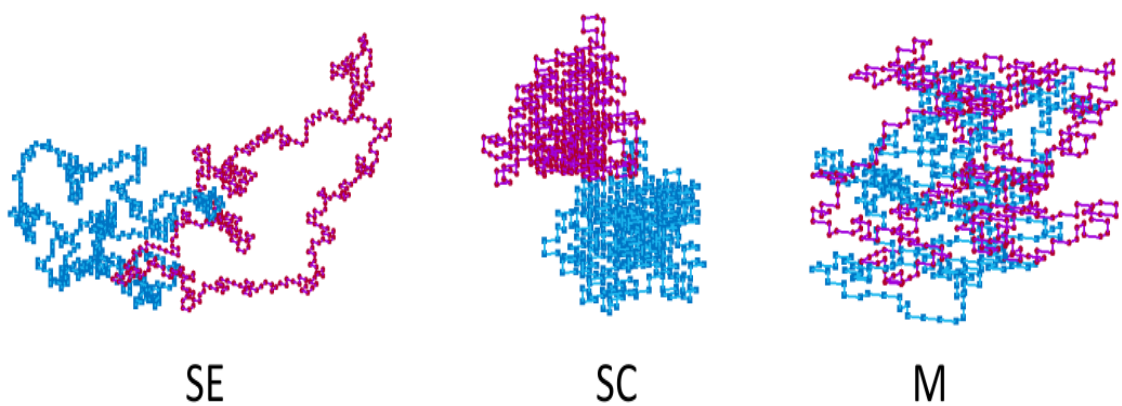

Figure 3: Examples of equilibrium configurations of $2n = 800$ sampled at $\beta_c = 0, \beta_m = 0$ (SE), $\beta_c = 0.5, \beta_m = 0$ (SC) and $\beta_c = 0, \beta_m = 0.75$ (M).

By Jensen's inequality

$$Z_{2n}(\beta_m, \beta_c)\, Z_{2n}(\beta_m', \beta_c') \geq \big(Z_{2n}((\beta_m + \beta_m')/2, (\beta_c + \beta_c')/2)\big)^2 \tag{5}$$

Taking logarithms, dividing by 2, gives

$$(1/2) \log Z_{2n}(\beta_m, \beta_c) + (1/2) \log Z_{2n}(\beta_m', \beta_c') \geq \log Z_{2n}((\beta_m + \beta_m')/2, (\beta_c + \beta_c')/2). \tag{6}$$

By the midpoint theorem [22] it follows that $\log Z_{2n}(\beta_m, \beta_c)$ is a convex function of (β_m, β_c). Dividing by $2n$ and taking $n \to \infty$ gives the following theorem.

Theorem 2. *If $\beta_m < \beta_m^*(\beta_c)$ then the free energy $\phi(\beta_m, \beta_c)$ is a convex function. More generally, defining*

$$\limsup_{n\to\infty} \frac{1}{2n} \log Z_{2n}(\beta_m, \beta_c) = \phi(\beta_m, \beta_c)$$

is consistent with the definition of $\phi(\beta_m, \beta_c)$ in theorem 1, and moreover, $\phi(\beta_m, \beta_c)$ is a convex function for all (β_m, β_c). □

We notice that the limsup in theorem 2 is convex by dividing equation 6 by n and taking the limsup $n \to \infty$. Defining

$$\psi(\beta_m, \beta_c) = \liminf_{n\to\infty} \frac{1}{2n} \log Z_{2n}(\beta_m, \beta_c) \tag{7}$$

observe that $\phi(\beta_m, \beta_c) = \psi(\beta_m, \beta_c)$ for all $\beta_m < \beta_m^*(\beta_c)$. It follows that $\psi(\beta_m, \beta_c)$ is monotonic non-decreasing in β_m and β_c, and so it is differentiable almost everywhere. Taking the left-limit as $\beta_m \nearrow \beta_m^*(\beta_c)$ shows that

$$\lim_{\beta_m \nearrow \beta_m^*(\beta_c)} \psi(\beta_m, \beta_c) = \phi(\beta_m^*(\beta_c), \beta_c), \tag{8}$$

by the squeeze theorem for limits. This shows that in the statement of theorem 2 we can take $\beta_m \leq \beta_m^*(\beta_c)$.

We do not know that $\kappa_d(\beta_c)$ is not analytic, rigorously, at a collapse critical point β_c^0. However, if a collapse transition exists at $\beta_c = \beta_c^0$, then $\kappa_3(\beta_c)$ is non-analytic at β_c^0. It then follows from Theorem 1 that $\phi(\beta_m, \beta_c)$ is also not analytic at β_c^0 for all $\beta_m \leq \beta_m^*(\beta_c^0)$. This shows that, if the collapse transition exists, then the phase boundary separating the SE and SC phases in figure 2 must be a straight line. It is not known that the phase boundary separating the SE and M phases is a straight line.

4 Monte Carlo method

Using a Markov chain Monte Carlo algorithm, we sampled the equilibrium conformations of the diblock lattice copolymer model from the Boltzmann distribution defined by equation 3. The elementary moves were a combination of pivot moves for self-avoiding polygons that ensure ergodicity [17] and local Verdier-Stockmayer style moves [16] that increase the mobility of the Markov Chain, especially when the sampling is performed in the regions of large positive values of the interaction parameters β_m and β_c [14, 12].

Sampling was also improved by implementing the elementary moves using a Multiple Markov Chain algorithm [13, 14, 12] with parallel chains distributed along a sequence of parameters $(\beta_c(j), \beta_m(j))$ for $j = 1, 2, \ldots, M$. Along each parallel chain Metropolis sampling [15] was implemented to sample from the Boltzmann distribution at a fixed pair of values $(\beta_c(j), \beta_m(j))$, and chains were swapped using the protocols of Multiple Markov Chain (MCC) sampling [23, 14, 12].

The stationary distribution of the MCC implementation is the product of the Boltzmann distributions along each chain (see reference [14, 12]). The main difficulty in the practical implementation of the MMC scheme is the choice of the sequence of parameter pairs $(\beta_c(j),)\beta_m(j)), j = 1, 2, \ldots, M$. This is because the contiguous pairs $(\beta_c(j),)\beta_m(j))$ and $(\beta_c(j+1),)\beta_m(j+1))$ should be sufficiently close to allow a non-negligible number of swaps between them to occur. Swaps between chains were proposed at a rate proportional to the system size ($2n$ – that is the total combined length of the pair of polygons, for $n = 48, 100, 148, 200, 300, 400$).

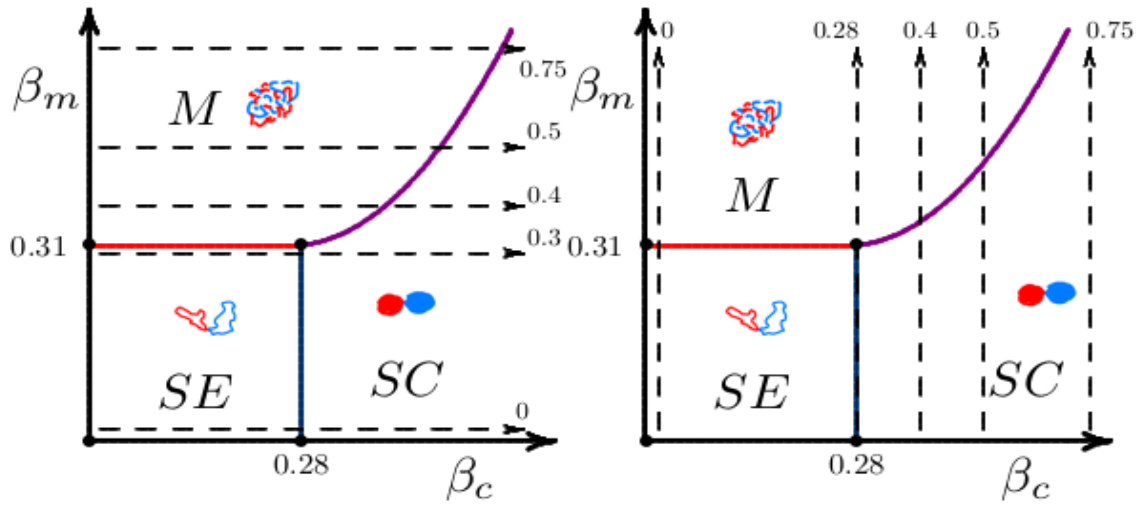

Figure 4: Crossing the M-SC boundary by keeping fixed $\beta_m > \beta_m^*(0)$ and varying β_c (left) or by keeping fixed $\beta_c > \beta_c^0$ and varying β_m (right).

We proceeded by collecting data of the metric and thermodynamic properties of the model along the chains by either fixing β_m and varying β_c or fixing β_c and letting β_m vary. More specifically, we choose a set of values of β_m at fixed β_c or a set of values of β_c at fixed β_m which samples the relevant region of the phase diagram and crosses the expected phase boundaries previously described.

For most cases we used $M \approx 25$ parallel chains, and we were able to obtain sufficiently uncorrelated samples for systems of *total* size $2n \in \{96, 200, 296, 400, 600, 800\}$. We counted a single iteration as $O(1)$ pivot moves, and $O(n)$ local Verdier-Stockmayer style moves. By spacing the reading of data along each Markov chain, we were able to sample approximately 2.5×10^4 conformations that are essentially *uncorrelated* at each fixed value of the pair $(\beta_c^{(j)}, \beta_m^{(j)})$ for a total of at least 1.25×10^6 data points for each value of n. The simulations were expensive in terms of CPU time. For example, for $2n = 800$ (each polygon in the pair has length 400) and $M \approx 25$, a total of 25,000 uncorrelated conformations were sampled over two months of CPU time on an $x86_64$-based workstation. In figure 3 we show some examples of conformations taken along the chains for different values of the pair $(\beta_c^{(j)}, \beta_m^{(j)})$.

To explore the phase diagram we primarily carried out simulations as shown in figure 4. In the first instance we fixed β_m at values in $\{0, 0.2, 0.3, 0.4, 0.5, 0.75\}$ and collected data along Markov chains for $\beta_c \in [0, 1]$. This is shown by the arrows crossing the SE-SC and M-SE phase boundaries in the left panel of figure 4. For example, the SE-SC phase boundary was explored fixing β_m at values 0, 0.2 and 0.3. In the right panel we fixed β_c instead at the values $\{0, 0.2, 0.28, 0.4, 0.5, 0.75\}$ respectively, while varying β_m to cross the SE-M and SC-M phase boundaries.

5 Numerical results

In this section we explore in more detail the phase diagram illustrated in figure 2 using Monte Carlo simulations. We will in particular focus on the phase boundaries and the thermodynamic properties of the three phases.

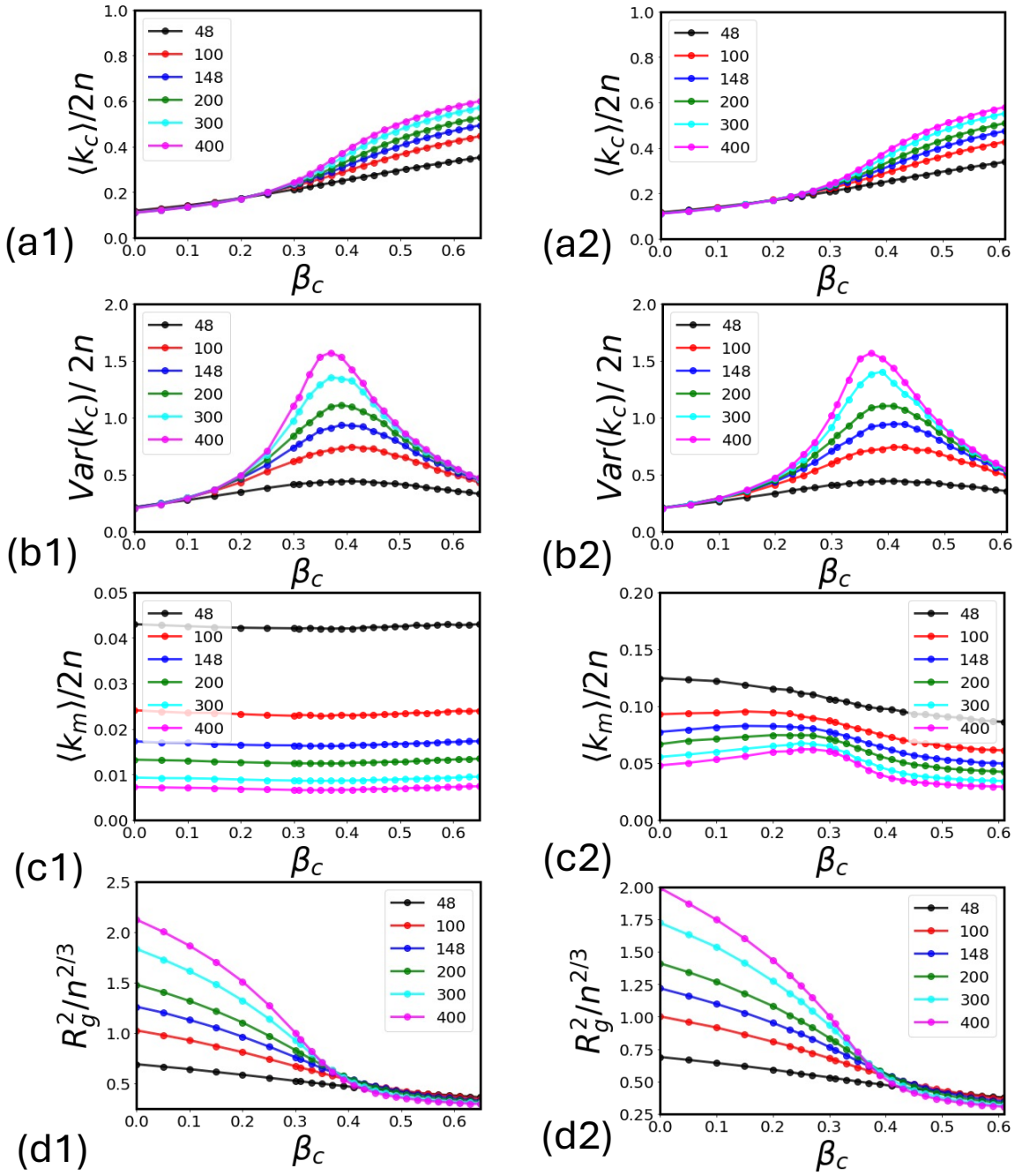

Figure 5: (a1-a2) The average number of self contacts scaled by length, $\langle k_c \rangle/2n$, as a function of β_c. Different symbols colours correspond to different system sizes (see the legends). (b1-b2) Plots of the corresponding variance of k_c scaled by the system's size, $Var(k_c)/2n$, as a function of β_c. (c1-c2) Corresponding plots of the average number of mutual contacts scaled by $2n$, $\langle k_m \rangle/2n$, as a function of β_c. (d1-d2) Plots of the mean-squared radius of gyration of the single components, $\langle R_g^2 \rangle$, scaled by $n^{2/3}$, as a function of β_c. The two columns correspond to simulations performed at the fixed values of $\beta_m = 0$ and 0.30 respectively.

5.1 The SE-SC phase boundary

Consider first the case that $\beta_m = 0$. In this event the only nearest-neighbour self-attraction between monomers is when $\beta_c > 0$. In the event that $\beta_c \leq 0$ the model is in a phase of segregated and expanded polygons. Increasing $\beta_c > 0$ the model is expected to undergo a collapse transition at the θ-point at a critical value $\beta_c^0 > 0$. In the case of cubic lattice polygons $\beta_c^0 \approx 0.278$ [12, 11], and one expects this to be also the location of the θ-point in our model when $\beta_m \leq 0$.

In the top row of graphs in figure 5 the average number of self-contacts per unit length $\langle k_c \rangle / 2n$, for polygons of length n, is plotted as a function of $\beta_c \in [0, 0.65]$. The values of n increase from $n = 48$ to $n = 400$, and the panels correspond to fixed values of $\beta_m = 0$ (panel a1) and $\beta_m = 0.3$ (panel a2). The data in the two panels consistently show linear growth of $\langle k_c \rangle$ for $\beta_c \lesssim 0.3$ and superlinear growth when $\beta_c \gtrsim 0.3$.

If $\beta_m = 0$ then the model is composed of two polygons modelling ring polymers in a good solvent. It can be shown that the connective constant of the pair of polygons is equal to that of a single polygon. In the case of a single polygon the pattern theorem [18] shows that $\langle k_c \rangle$ grows at least linearly with n. The linear growth seen in figure 5(a1) is then consistent with an expanded phase in the model. The superlinear growth in n for large β_c indicates nearest neighbour contacts between vertices far apart along the polygon backbones – this is consistent with compact conformations. This change in behaviour at a critical point β_c^0 is consistent with a θ-point transition and the locations at which the curves deviate from linear behaviour as finite-size estimates of the phase boundary. The variances $Var(k_c) = \langle k_c^2 \rangle - \langle k_c \rangle^2$ for the same fixed values of β_m are shown in figure 5(b1-b2). As n increases the locations of the peaks shift towards lower values of β_c while their height increases. The peaks are finite size effects observed due to a singularity in the thermodynamic limit.

The panels in figure 5(c1-c2) show the average number of mutual contacts per unit length, denoted $\langle k_m \rangle / 2n$. This decreases with increasing n and may approach zero as $n \to \infty$, indicating that the model is in a segregated phase for the entire range of β_c in the simulation.

In the segregated phases one may distinguish between the extended and the compact phases by examining the scaling behaviour of the mean squared radius of gyration $\langle R_g^2 \rangle$. In the extended phase it is known that $\langle R_g^2 \rangle \sim n^{2\nu}$ with $\nu = 0.587...$ [24]. In the compact phase one expects that $\langle R_g^2 \rangle \sim n^{2/3}$. That is, the curves $\langle R_g^2 \rangle / n^{2/3}$ plotted against β_c should increase with n for $\beta_c < \beta_c^0$, but inside the compact phase they should be independent on n. This behaviour is confirmed in figures 5(d1-d2). In the compact phase the curves do not fully collapse onto a unique curve but show a slight decrease with n. Nevertheless, the curves cross one another and we consider the location of these crossings as a further finite-size estimate of the SE-SC phase boundary.

In figure 6(a) we plot the estimated locations of the maxima in the variances $Var(k_c)/2n$. These maxima were estimated using a fourth order spline fit to the data points. We plot these maxima against $1/\sqrt{n}$ (at the θ-point the finite size crossover exponent ϕ is expected to have its mean field value 1/2). The crossings between the scaled mean square radius of gyration curves $\langle R_g^2 \rangle / n^{2/3}$ for $n = 400$ with the corresponding curves estimated for $n = 48, 100, 148, 200$ and 300 are plotted in figure 6(b). The thick segment at $1/\sqrt{n} = 0$ in the two graphs marks the estimated location of the cubic lattice θ-point $\beta_c^0 = 0.2782 \pm 0.007$ in reference [12]. Observe that (i) the $n \to \infty$ extrapolations of the data in both graphs are very close to previous estimates of the cubic lattice θ transition; and (ii) the phase boundary between the SE and SC phases seems to be independent of the strength of the mutual attraction β_m, at least in the range $\beta_m \in [0, \beta_m^*(0)] \approx [0, 0.31]$.

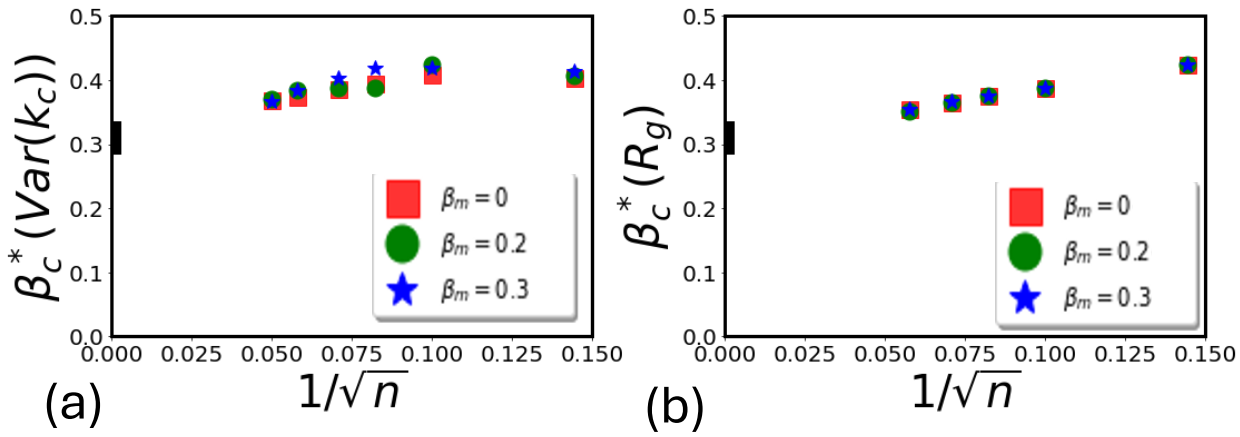

Figure 6: Estimating the location of the critical point β_c^0 from the locations of peaks in $Var(k_c)$ (denoted by $\beta_c^*(Var(k_c))$) and the locations of crossing points of mean square radius of gyration curves (denoted by $\beta_c^*(R_g)$) – see figure 5 panels (b1) and (b2), and panels (d1) and (d2). (a) The locations of the peaks of $Var(k_c)/2n$ for three values of the mutual attraction parameter $\beta_m = 0.0, 0.20, 0.30$. (b) The corresponding locations of the crossings between the curve $\langle R_g^2\rangle/n^{2/3}$ vs β_c at $n = 400$ and the curves for $n = 48, 100, 148, 200$ and 300. The three values of β_m are the same as in (a). In both cases the data are plotted against $1/\sqrt{n}$. The vertical bar at $1/\sqrt{n} = 0$ refers to the estimate of β_c^0 reported for the standard θ-point in [12].

5.2 SE-M phase boundary

If $\beta_c = 0$ then the model reduces to two polygons with a mutual nearest neighbour attraction between vertices in different polygons. In this case the model goes through a segregated-mixed phase transition at $\beta_m^*(0) \approx 0.31$ [1]. The average number of mutual contacts per unit length, $\langle k_m\rangle/2n$, is shown as a function of β_m (for $\beta_c = 0$ and 0.28) in figure 7 for $n = 48, 100, 148, 200, 300$ and 400.

The first column corresponds to $\beta_c = 0$ and the second column to $\beta_c = 0.28$. The second row in figure 7 corresponds to the variance of k_m per unit length ($Var(k_m)/2n = (\langle k_m^2\rangle - \langle k_m\rangle^2)/2n$) and the last row is the distance d_m between the centres of mass of the two polygons.

The intersecting variance curves in the second row of graphs are consistent with a critical point corresponding to a transition into a mixed phase. The intersections are also consistent with the estimate $\beta_m^*(\beta_c) \approx 0.31$ for $\beta_c \in [0, \beta_c^0]$.

If $\beta_m < \beta_m^*(0)$ then $\langle k_m\rangle/2n$ tends to zero as n increases (this is seen in the left-most panel in the first row in figure 7). This behaviour persists also for $0 < \beta_c < \beta_c^0$ (as seen in the right-most panel in the top row of figure 7). These results are consistent with two polygons being segregated in space if $\beta_m < \beta_m^*(0)$. Notice that above a particular value of β_m the curves $\langle k_m\rangle/2n$ increase with n in the panels in the top row of figure 7. This increase in mutual contacts characterizes a mixed phase where the two components share the same region in space (when the model transitions as β_m increases beyond the critical point $\beta_m^*(0) \approx 0.31$ in figure 2 separating the SE- and M-phases).

The onset of a thermodynamic phase transition between the SE- and M-phases is also suggested by the β_m dependence of $Var(k_m)/2n$ in the curves in the middle row of panels in figure 7. Notice the onset of peaks whose heights increase with n. Moreover, the curves cross one another in a narrow region of the mutual interaction parameter β_m. This is consistent with the theorem that,

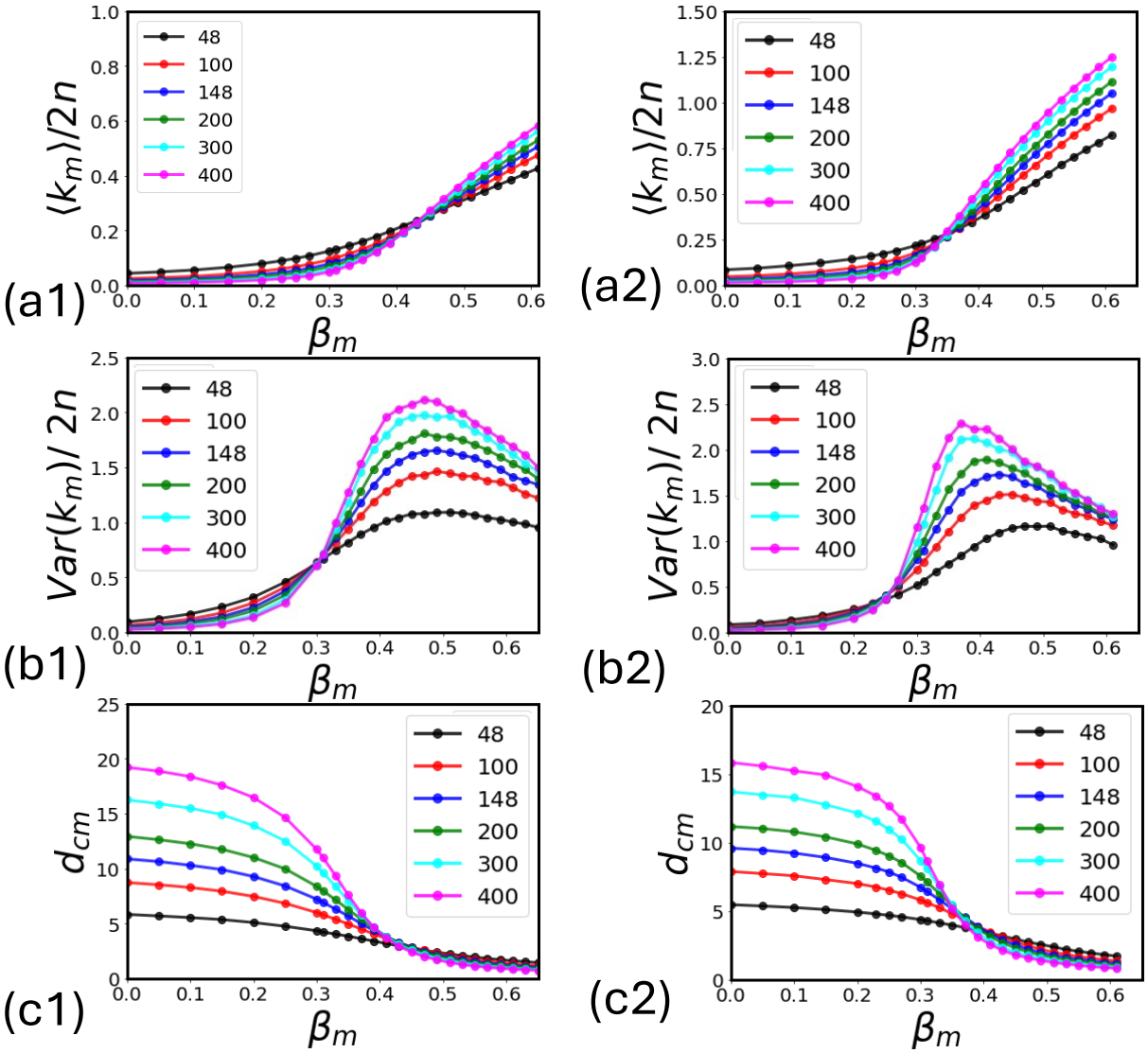

Figure 7: (a1-a2) Plots of the average number of mutual contacts scaled by $2n$, $\langle k_m \rangle/2n$, as a function of β_m. Different symbols refer to different system sizes (see legend). (b1-b2) Plots of the corresponding variance of k_m scaled by the system's size, $Var(k_m)/2n$, as a function of β_m. (c1-c2) Corresponding plots of the distance between the centre of mass of the two polygons d_{cm} as a function of β_m. The two columns correspond to simulations performed at the fixed values of $\beta_c = 0.0$ and 0.28 respectively.

for $\beta_c < \infty$, and $\beta_m < \beta_m^*(0)$, $\lim_{n\to\infty} Var(k_m)/2n = 0$; see section 3 and theorem 1. That result shows the presence of an asymmetric phase transition when $\beta_c < \infty$ somewhat similar to the adsorption transition of a self-avoiding walk anchored to an impenetrable attractive wall [25]. In these cases it is known that the intersections of the curves $Var(k_m)/2n$ plotted against β_m provide a faithful finite-size estimate of the location of the phase boundary [26].

A further indication of an SE-M phase boundary is seen in the behaviour of the distance between the centres of mass of the two components, d_{cm}, as a function of β_m (these data are plotted in the

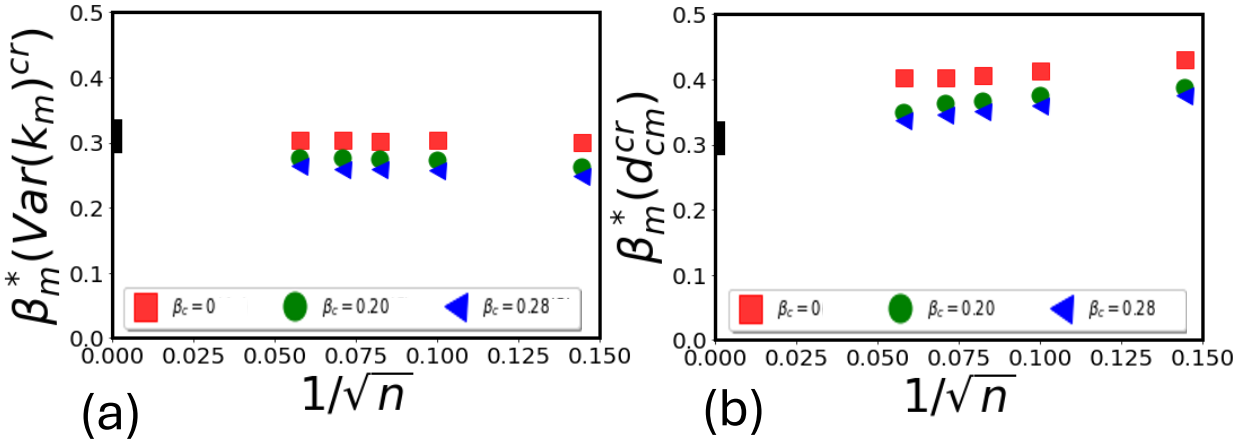

Figure 8: Determining the location of the critical point $\beta_m^*(0)$ from the locations of crossings between the $Var(k_m)$ curves (denoted by $\beta_m^*(Var(k_m)^{cr})$) and from the locations of crossing points of d_{cm} curves (denoted by $\beta_m^*(d_{cm}^{cr})$) – see figure 7 panels (b1) and (b2), and panels (c1) and (c2). (a) The locations of the crossings of the variance per unit length curves $Var(k_m)/2n$ as a function of $n = 400$ with the corresponding curves for $m = 48, 148, 200, 300$, (b) As in the left panel but for the curves d_{cm} against β_m. The three values of β_c are $0.0, 0.20$ and 0.28 (see legend). In both panels data have been plotted against $1/\sqrt{n}$. The vertical bar at $1/\sqrt{n} = 0$ is the estimate of $\beta_m^*(0)$ (see reference [1]) for the $\beta_c = 0$ case. These data appear to approach the critical point $\beta_m^*(0)$ as n increases.

bottom row panels in figure 7). In the SE phase, for $\beta_c = 0$, the hard-core repulsion between vertices in the two polygons induces an entropic repulsive force between the polygons, segregating them when $\beta_m < \beta_m^*(0)$. Here the natural length scale is n^ν, where ν is the metric exponent of the self-avoiding walk. This shows that $d_{cm} \sim n^\nu$ in the SE-phase. In the M-phase the two-component polygons share the same region as the attractive forces have overcome the entropic repulsion due to hard core nearest neighour interactions. In this case d_{cm} should approach a constant, or grow slowly with n at a rate slower than $O(n^\nu)$. These expectations are supported by the data in the left-most panel in the bottom row of figure 7, and the corresponding data for $\beta_c = 0.28$ seen in the other panel show consistent behaviour with $\beta_c = 0$, also indicating that the phase boundary between the SE- and M-phases in figure 2 is a straight line.

To determine the approximate location of the critical point $\beta_m^*(\beta_c)$ the crossings between the curves $Var(k_m)/2n$ and d_{cm} were determined and plotted against $1/\sqrt{n}$ in figure 8 (assuming the mean field value 1/2 for the finite size crossover exponent ϕ and plotting the intersections between the variance for $n = 400$ and for $n = 48, 100, 148, 200$ and 300). The data plausibly extrapolate to the value seen in reference [1], namely $\beta_m^*(0) \approx 0.31$ (the thick segment at $1/\sqrt{n} = 0$ marks the estimate of the expanded-mixed phase transition $\beta_m^*(0) = 0.31 \pm 0.01$ reported in reference [1]). A similar extrapolation is reported for the location of the crossings of the curve $d_{cm}(n = 400)$ with the corresponding curves obtained for $n = 48, 100, 148, 200$ and 300 in the last row of panels in figure 8. The limiting estimate shown by the thick segment at $1/\sqrt{n} = 0$ is again the expanded-mixed phase transition point $\beta_m^*(0) = 0.31 \pm 0.01$ reported in reference [1]. Similarly to the SE-SC phase boundary, we note that: (i) the $n \to \infty$ extrapolation of the points of both measures is very close to $\beta_m^*(0)$, and (ii) the SE-M phase transition appears to be independent of the strength β_c of

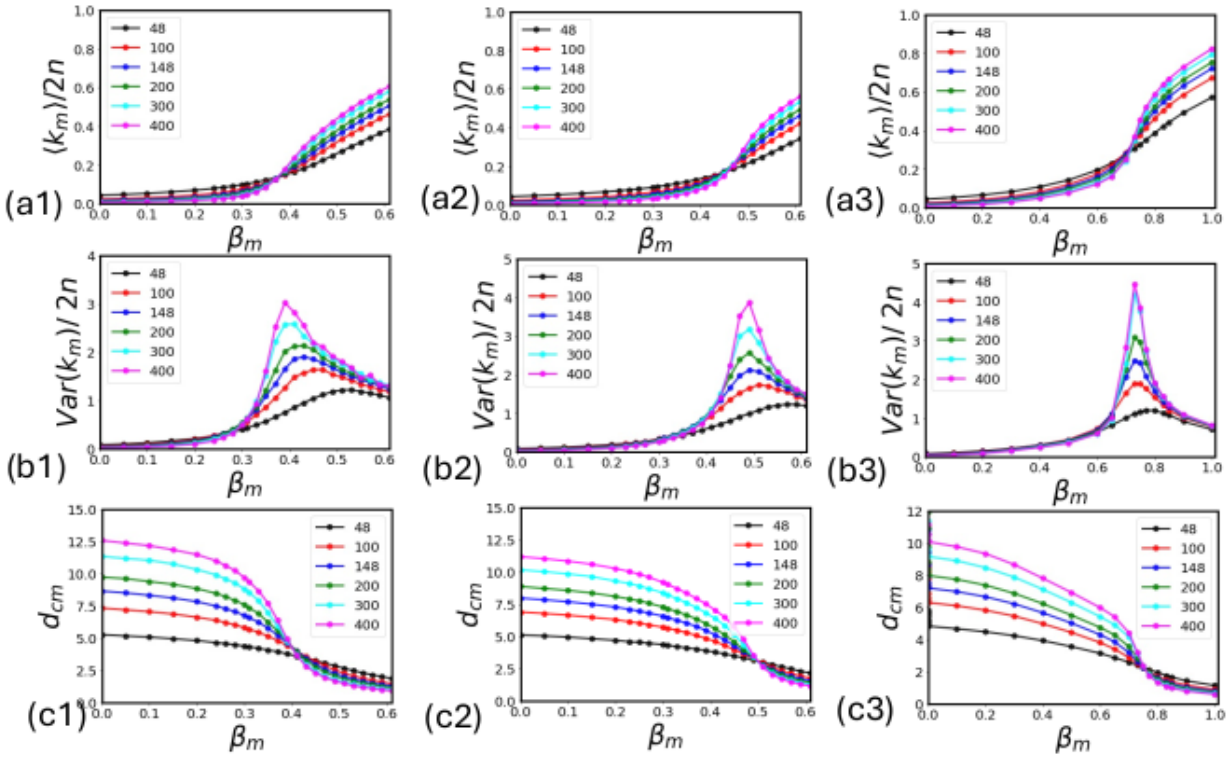

Figure 9: (a1-a3) Plots of the average number of mutual contacts per unit length, $\langle k_m \rangle/2n$, as a function of β_m for $\beta_c = 0.4, 0.5$ and 0.75. These values are well above the theta transition $\beta_c^0 \approx 0.28$ (see the right panel of figure 4). Different symbols refer to different system sizes (see the legend). (b1-b3) Plots of the variance per unit length, $Var(k_m)/2n$, as a function of β_m for the same fixed values $\beta_c = 0.4$, 0.5 and 0.75. (c1-c3) Corresponding β_m dependence of the distance between the centre of mass of the two polygons, d_{cm}.

the self attraction between vertices in the polygons, at least when $0 \leq \beta_c < \beta_c^0$.

5.3 The SC-M phase boundary

Next, we consider the phase diagram in the region $\beta_c > \beta_c^0$ and $\beta_m > \beta_m^*(0)$. We performed simulations crossing phase boundaries as shown in the right panel of figure 4 by keeping fixed the parameter β_c (mutual attractions) at values $\{0.4, 0.5, 0.75\}$ inside the SC phase while varying β_m across SC-M phase boundaries. A similar approach was followed to examine the M-SC boundary by varying β_c while keeping β_m fixed at the values $\{0.4, 0.5, 0.75\}$, following the corresponding arrows in the left panel of figure 4.

In figure 9 $\beta_c = 0.4$ in the first column, $\beta_c = 0.5$ in the second column, and $\beta_c = 0.75$ in the third column, while β_m varies from 0 to 1. In the first row of graphs we plot the average number of mutual contacts per unit length $\langle k_m \rangle/2n$, in the second row the variance of k_m per unit length, $Var(k_m)/2n$, is plotted, and in the third row the separation d_{cm} between the centres of mass of the component polygons is plotted.

Similar to the SE-M phase boundary (see section 5.2) the graphs in figure 9 shows the presence of finite-size phase behaviour at a critical value of β_m. The location of the phase boundary can be estimated by again examining crossings between the curves for the variance and d_{cm} in figure 9.

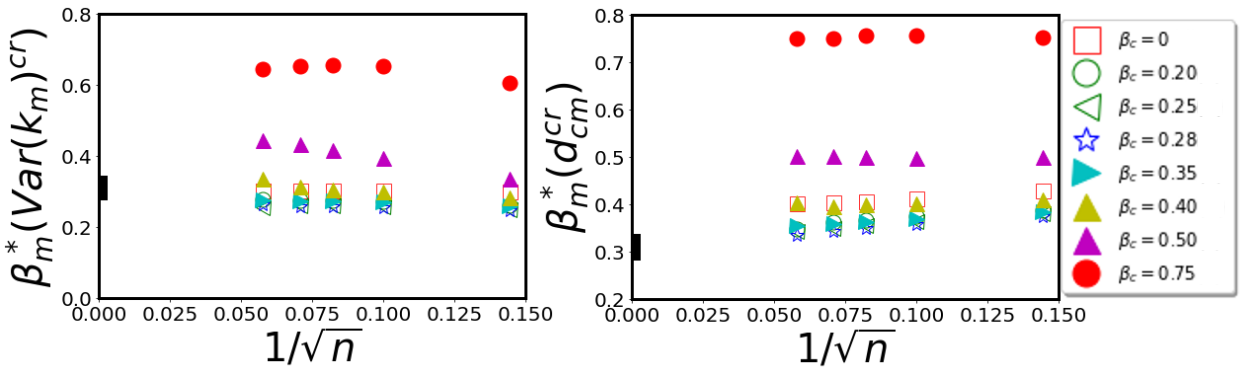

Figure 10: Determining the locations of points on the critical curve $\beta_m^*(\beta_c)$ by extrapolating the locations of crossings between the $Var(k_m)$ curves (denoted by $\beta_m^*(Var(k_m)^{cr})$) and extrapolating the locations of crossing points of d_{cm} curves (denoted by $\beta_m^*(d_{cm}^{cr})$) – see figure 7 panels (b1) and (b2), and panels (c1) and (c2). and figure 9 panels (b1), (b2) and (b3), and panels (c1), (c2) and (c3). Left panel: The locations of crossings $\beta_m^*(Var(k_m)^{cr})$ between the curve $Var(k_m)/2n$ for $n = 400$ (see the middle row of figure 9) and $Var(k_m)/2n$ for $n \in \{48, 100, 148, 200, 300\}$ for values of $\beta_c < \beta_c^0$ (below the θ-point; these are the empty symbols) with those above β_c^0 (solid symbols). The locations are plotted as a function of $1/\sqrt{n}$. Notice that the data below the θ-point tends to line up and extrapolate as $n \to \infty$ to the marked solid vertical bar at $1/\sqrt{n} = 0$ (this is the estimate for β_m^* in reference [1] for the case $\beta_c = 0$. In contrast, the data above the θ-point extrapolate to larger values on the vertical axis. Right panel: This is similar to the left panel, but now for the curves d_{cm} in the middle row of figure 9. The values of β_c are reported in the legend.

These are plotted in figure 10 (the left panel is the data determined from $Var(k_m)$ and the right panel corresponds to the results from d_{cm}). The data for $\beta_c = 0, 0.2, 0.3$ are also included for reference in the graphs (see figure 8) – these are the empty symbols. Notice that these empty symbols coincide within statistical uncertainty for different values of $\beta_c = 0, 0.2, 0.3$, but that when $\beta_c > \beta_c^0$ then the data (the filled-in symbols) spread to larger values of β_m. This trend is seen in both the left and right panels of figure 9. In figure 10, for $\beta_c = 0.5$, the data extrapolate (purple triangles for $\beta_c = 0.5$) to $\beta_m^*(0.5) \approx 0.5$, while for $\beta_c = 0.75$ the data (red circles) seem to extrapolate to $\beta_m^*(0.75) \approx 0.75$. The case $\beta_c = 0.4$ (yellow/green triangles) is more delicate since it is closer to the line of θ-points along the SE-SC phase boundary separating the SE-M and SC-M phase boundaries. The results in the right panel apparently extrapolating to a value $\beta_m^*(0.4) \approx 0.4$ when $\beta_c = 0.4$.

5.4 The M-SC phase boundary

In this section we consider data along lines crossing from the mixed into the segregated-collapsed phase as illustrated in the left panel of figure 4. In this case β_m is fixed at one of $\{0.4, 0.5, 0.75\}$, while β_c is increased in the interval $[0, 1]$. In this case a phase boundary between the M and SC phases should be crossed. Our simulations tracked the observables plotted in figure 11. The left column of panels corresponds to $\beta_m = 0.4$, the middle column to $\beta_m = 0.5$, and the right column to $\beta_m = 0.75$. In this case the data are plotted as a function of $\beta_c \in [0, 0.75]$.

The following results are observed:

Density of contacts k_c: The density of nearest neighbour contacts $\langle k_c \rangle / 2n$ is plotted in the top

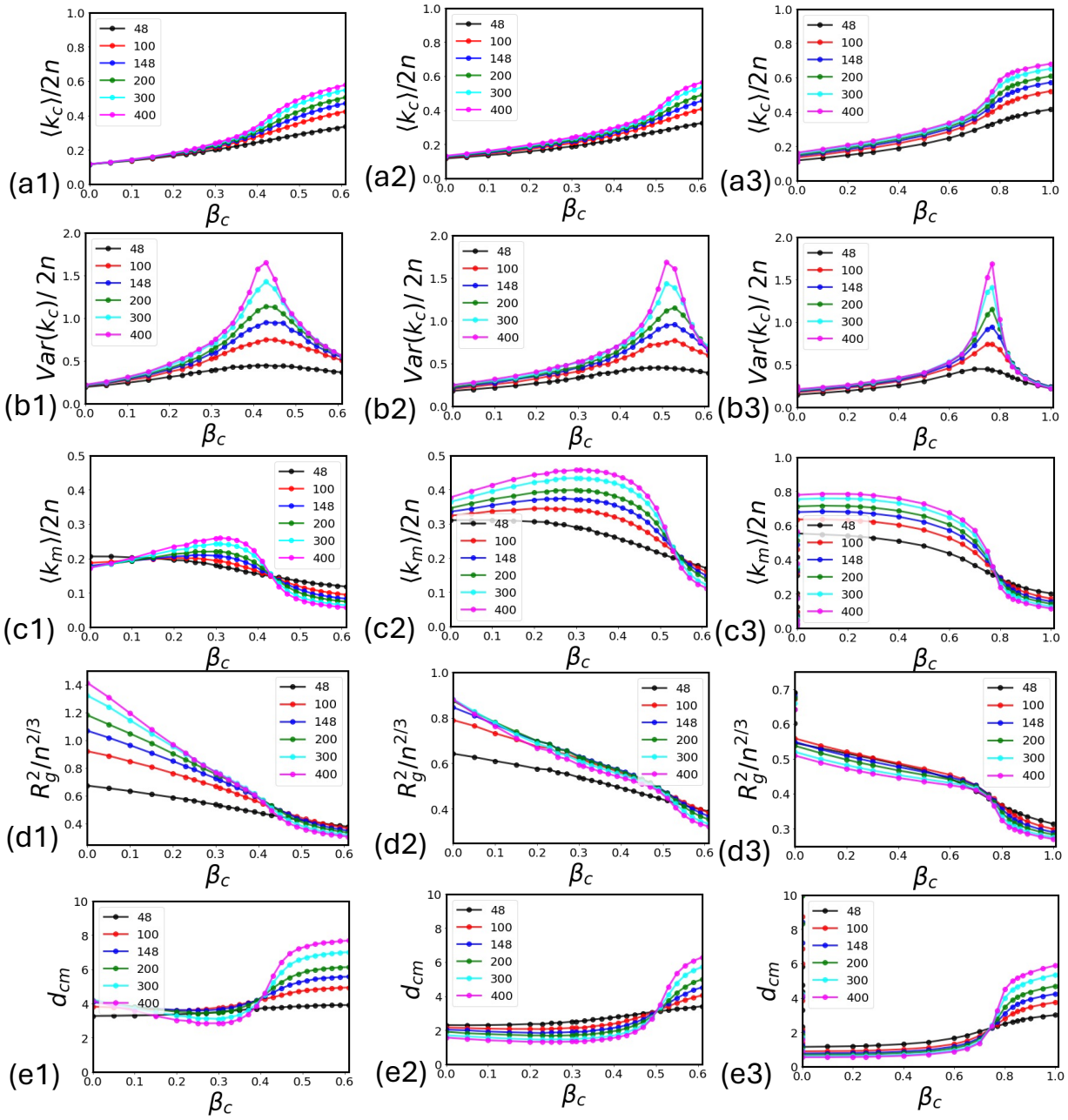

Figure 11: (a1-a3) The average number of self-contacts scaled by the system's size, $\langle k_c \rangle/2n$, as a function of β_c. (b1-b3) Variance of k_c scaled by the system's size, $Var(k_m)/2n$, as a function of β_c. (c1-c3) The average number of mutual contacts scaled by the system's size, $\langle k_m \rangle/2n$, as a function of β_m. (d1-d3) β_m dependence of the mean-squared radius of gyration of one component, R_g^2, scaled by $n^{2/3}$. (e1-e3) Corresponding plots of the distance between the centre of mass of the two polygons, d_{cm}, as a function of β_m. Different symbols refer to different system sizes (see legend). The three columns $(1, 2, 3)$ correspond to simulations performed at the fixed values of $\beta_m = 0.40, 0.50, 0.75$, respectively.

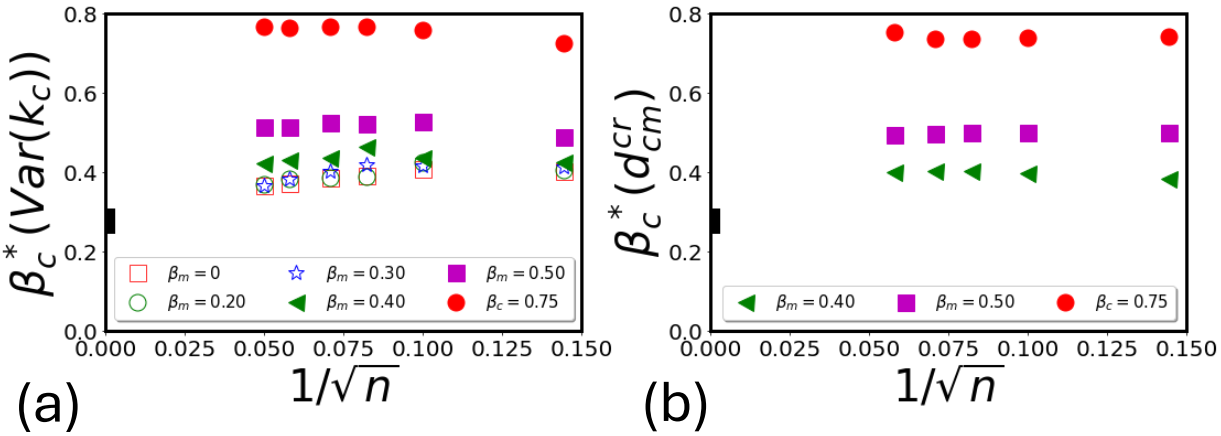

Figure 12: Determining the locations of points on the critical curve $\beta_m^*(\beta_c)$ by extrapolating the locations of peaks in the $Var(k_c)$ curves (denoted by $\beta_c^*(Var(k_c))$ and extrapolating the locations of crossing points between d_{cm} curves (denoted by $\beta_c^*(d_{cm}^{cr})$) – see figure 11 panels (b1), (b2) and (b3), and panels (e1), (e2) and (e3). (a) Comparison of the locations of the maxima of the variance curves $Var(k_c)/2n$ for various values of β_m. These data plausibly extrapolate to β_c^0 for data below the M-SE transition (this corresponds to the empty symbols), but to larger values above the M-SE transition (solid symbols). (b) Similar to (a), but now for the separation between the centre-of-mass data d_{cm} plotted for various values of β_m. The values of β_m are reported explicitly in the legend. In both panels data have been plotted as a function of $1/\sqrt{n}$. The vertical bars at $1/\sqrt{n} = 0$ refers to the estimates of β_c^0 provided in equation 1.

row of panels in figure 11. Here, the β_c dependencies are similar to what was observed as we crossed the SE-SC boundary in the top row of panels in figure 5.

Variance of k_c: The variance develops a peak consistent with the location of the M-SC phase transition, and this peak grows with n similarly to the peaks seen in the second row of panels in figure 5. Moreover, the data show that k_c is a sensitive indicator for detecting the transition across the M-SC phase boundary.

Density of mutual contacts k_m: The β_c dependence of $\langle k_m \rangle / 2n$ has a more interesting profile than observed across the SE-SC boundary in the third row of panels in figure 9. The curves have non-monotonic behaviour in the mixed phase with increasing β_c, first increasing for small β_c, but then decreasing as the M-SC phase boundary is approached and then crossed. This behaviour is due to competition between self- and mutual contact interactions. As β_c increases in the mixed phase, the component polygons contract, creating more mutual and self-contacts. In the SC phase more self-contacts are formed to the exclusion of mutual contacts. We also notice that the curves intersect at a particular point insensitive to system size n. This can be used to determine the location of the M-SC phase boundary.

Radius of gyration: Unlike the SE-SC boundary the behaviour of R_g is less clear. It generally decreases with increasing β_c, as expected. However, the scaling seems to have significant finite-size corrections. For instance, at $\beta_m = 0.4$ it does not scale proportionally to $n^{2/3}$. This suggests that the M phase is not a compact collapsed regime. As β_c increases, crossing the M-SC phase boundary, the expected $n^{2/3}$ behaviour appears to emerge. In the case of larger

values of β_m the curves in the middle and right panels collapse over the entire range of β_c at larger values of n, suggesting that the $n^{2/3}$ scaling emerges and the phase has characteristics of a collapsed phase.

Distance between the two centres of mass: These are plotted in the bottom row of panels in figure 11. The corresponding curves show non-linear behaviour, increasing as the M-SC phase boundary is crossed. In the M phase the polygons are interpenetrating each other, resulting in a smaller separation d_{cm}. Crossing into the SC phase increases the separation, as one would expect. The non-linear behaviour of d_{cm} with increasing β_c in the M phase is more difficult to explain, but there is a competition between mutual and self-contacts. Increasing β_c from a small value in the M phase would contract the component polygons, also increasing the mutual contacts. However, as β_c increases, self-contacts are formed at the cost of mutual contacts, tending to separate the polygons more as the critical M-SC phase boundary is approached.

Estimates of the location of the M-SC phase boundary, based on peaks in the $Var(k_c)$ curves and the crossings between d_{cm} curves are plotted in figure 12. These points are again plotted against $1/\sqrt{n}$, and the vertical bar on the y-axis is the confidence interval of estimate of β_m^* in reference [1] when $\beta_c = 0$.

6 Topological entanglement

In the previous sections we have seen that the two polygons have distinct metric and thermodynamic properties in the various thermodynamic phases in figure 2. For example, in the mixed phase, the model is characterised by the mixing of the polygons, increasing mutual contacts. Characteristic in this phase is that the pair of polygons is reduced in size with an increased local density of monomers inside the convex hull of the pair. This increased density should also increase entanglements between strands of the two polygons, increasing the probability that they are catenated into a non-trivial topological link.

In contrast, steric repulsion between monomers in the segregated phases should make linking of the two components less likely. In the segregated-expanded phase, the two components are separated from each other, and this should also reduce the probability that each of the components is knotted (in addition to the two components being unlikely to form a non-trivial link). In the segregated and collapsed phase, the two components remain separated, and so again are unlikely to form a non-trivial link. However, each component is now compacted and more likely to be knotted.

Thus, the (statistical) topological properties, as measured by the knotting of the components or the linking between components, change as the two rings cross phase boundaries. In any given phase, the topological properties may vary continuously, but one expects sudden changes across phase boundaries. To explore these expectations, we analysed the linking and knotting in the model as β_m changes while β_c is kept fixed, or vice versa.

Linking between the A- and B-blocks is computed via the two-variable Alexander polynomial $\Delta(t, s)$ [27] while knot detection is based on the computation of the Dowker code [28].

Since their computation would be prohibitively costly when the number of crossings n_c after a planar projection is very large, we first simplify the geometrical entanglement of the system while keeping its topology unaltered [29]. This is achieved by shrinking stochastically the polygons with the BFACF algorithm, simulated at a very small step fugacity K [30, 31, 32]. The BFACF moves

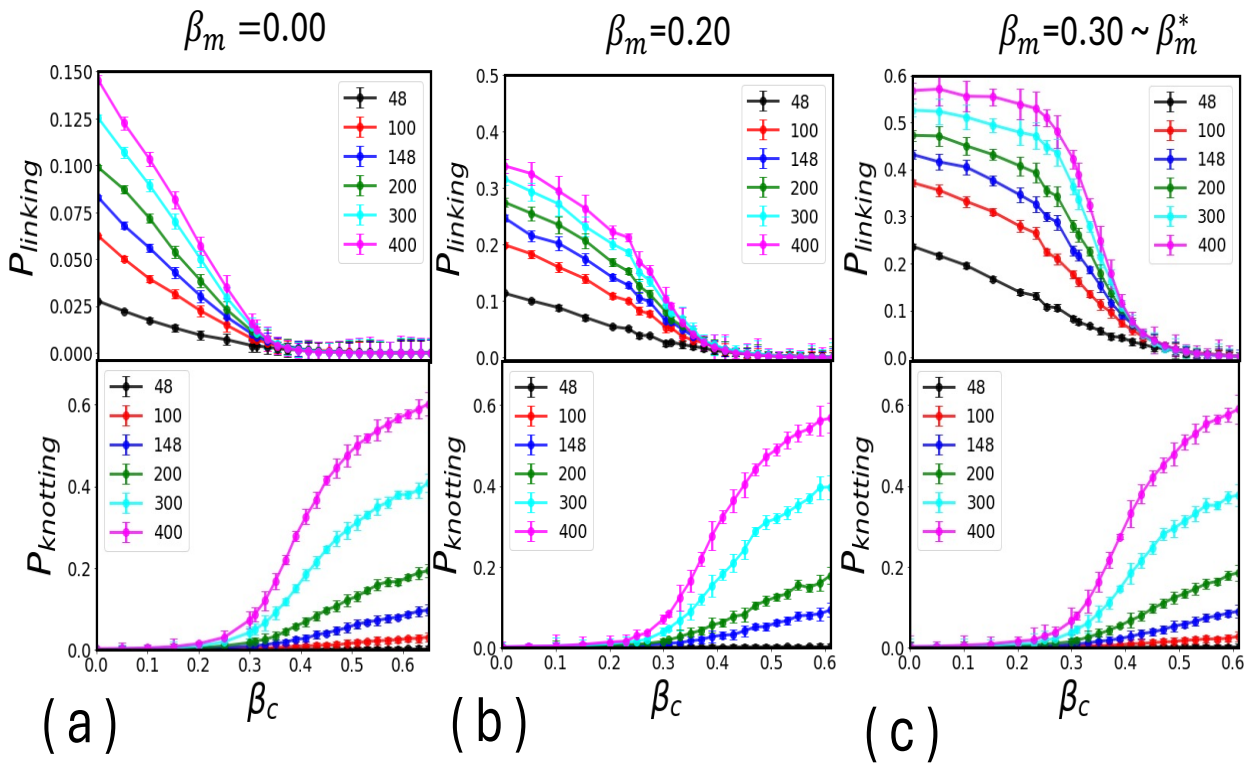

Figure 13: Topological entanglement as the SE-SC phase boundary is crossed by varying β_c: Linking probability (top row) and knotting probability (bottom row) as a function of the self-attraction parameter β_c for three fixed values of the mutual interaction parameter β_m, (a) 0.00, (b) 0.20 and (c) 0.30. Note that $\beta_m = 0.30$ is very close to the estimate of the transition point β_m^* when $\beta_c = 0$.

have the property of preserving the topology and, if K is sufficiently small, the system will often eventually shrink to its minimal length compatible with its topology. Even if the minimal length is not always reached, the shrunk configuration, once projected onto a plane, displays, most of the time, a sufficiently small number of crossings (well below 50) to dramatically reduce the time required to compute the topological invariants [29, 33].

6.1 Fixing β_m and varying β_c

In this section we fix β_m while increasing β_c. The values of β_m are chosen as illustrated in the left panel of figure 4 and the trajectories in the phase diagram crossing the SE-SC phase boundary when $\beta_m \in \{0, 0.2, 0.3\}$ and the M-SC phase boundary when $\beta_m \in \{0.4, 0.5, 0.75\}$.

In figure 13 the linking and knotting properties of the model are explored for $\beta_m \in \{0, 0.2, 0.3\}$ so that the SE-SC phase boundary is crossed when β_c increases beyond the critical point $\beta_c^0 \approx 0.28$. In the SE phase (the top row of panels in the figure for $\beta_c < \beta_c^0$) the components are linked with positive probability, increasing as the length of the polygons increases and as β_m approaches from below the transition value $\beta_m^*(\beta_c)$. Increasing β_c reduces the probability of linking to zero in the SC phase. This behaviour is expected, as the two components are segregated and compact in this

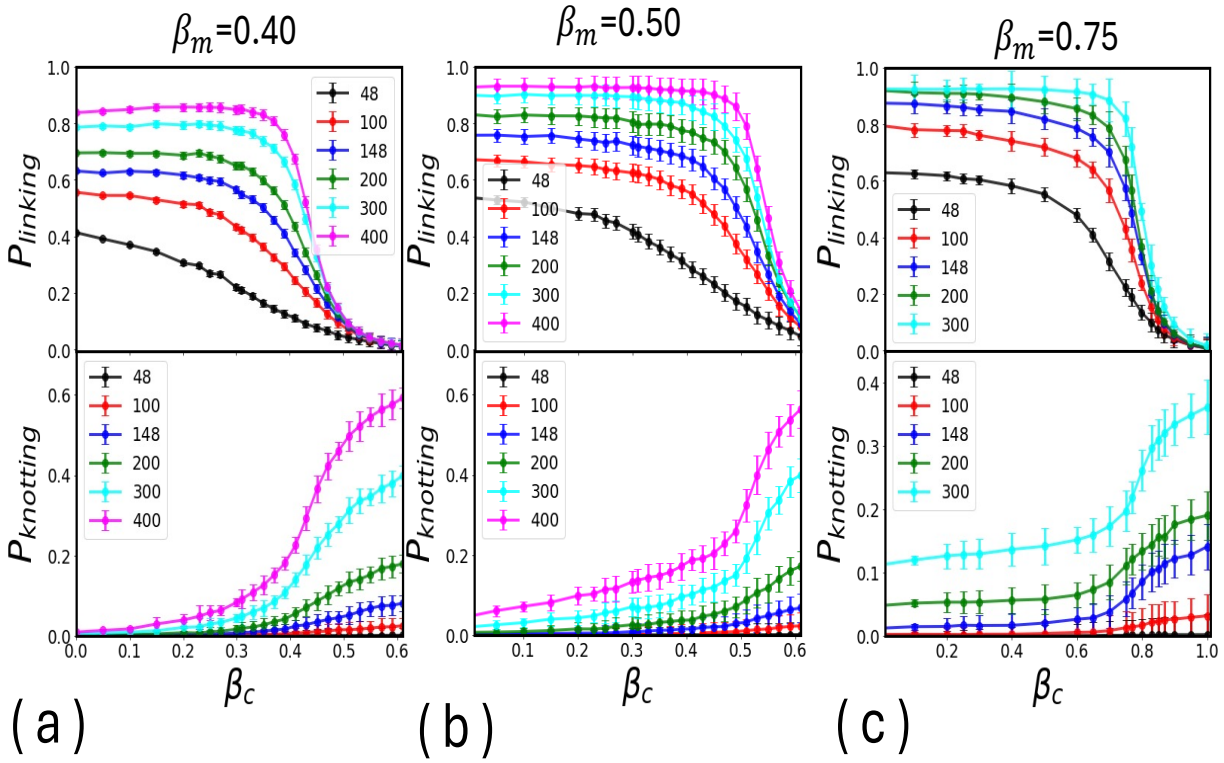

Figure 14: Topological entanglement as the M-SC phase boundary is crossed by varying β_c: Linking probability (top row) and knotting probability (bottom row) as a function of the self-attraction parameter β_c for three fixed values of the mutual interaction parameter β_m, (a) 0.40, (b) 0.50 and (c) 0.75. All values of β_m correspond to the system well inside the mixed phase.

phase, excluding each other and so making linking unlikely. In contrast, in the SE phase, the two polygons, although segregated, are also expanded, allowing strands of one to enter the other and to become entangled, giving rise to a positive probability of topological linking between the two components.

Knotting of the component polygons should increase when the SE-SC phase boundary is crossed, and this is seen in the bottom row of panels in figure 13. The knotting probability increases from a small value to significant values in the SC phase, consistent with previous studies showing low knotting probabilities of expanded polygons in the cubic lattice, which increase rapidly as the θ-point is crossed into a phase of collapsed polygons [8, 34].

In figure 14 we show similar data, but when the M-SC phase boundary is crossed by fixing β_m and increasing $\beta_c \in (0, 1.0)$ (where $\beta_m \in \{0.4, 0.5, 0.75\}$. In the M phase, the two polygons are mixed, and so we expect enhanced probabilities of linking. This is clearly evident in the top row of panels of figure 14 and can be seen by comparing the data to the corresponding panels in figure 13. In addition, as the M-SC phase boundary is approached, the linking probabilities in these figures decrease quickly into the SC phase. The results on knotting shown in the bottom row of panels in figure 14 are consistent with what is seen for the SE-SC transition in figure 13. The knotting probability is low and not much increased in the M phase, compared to the SE phase, but increases

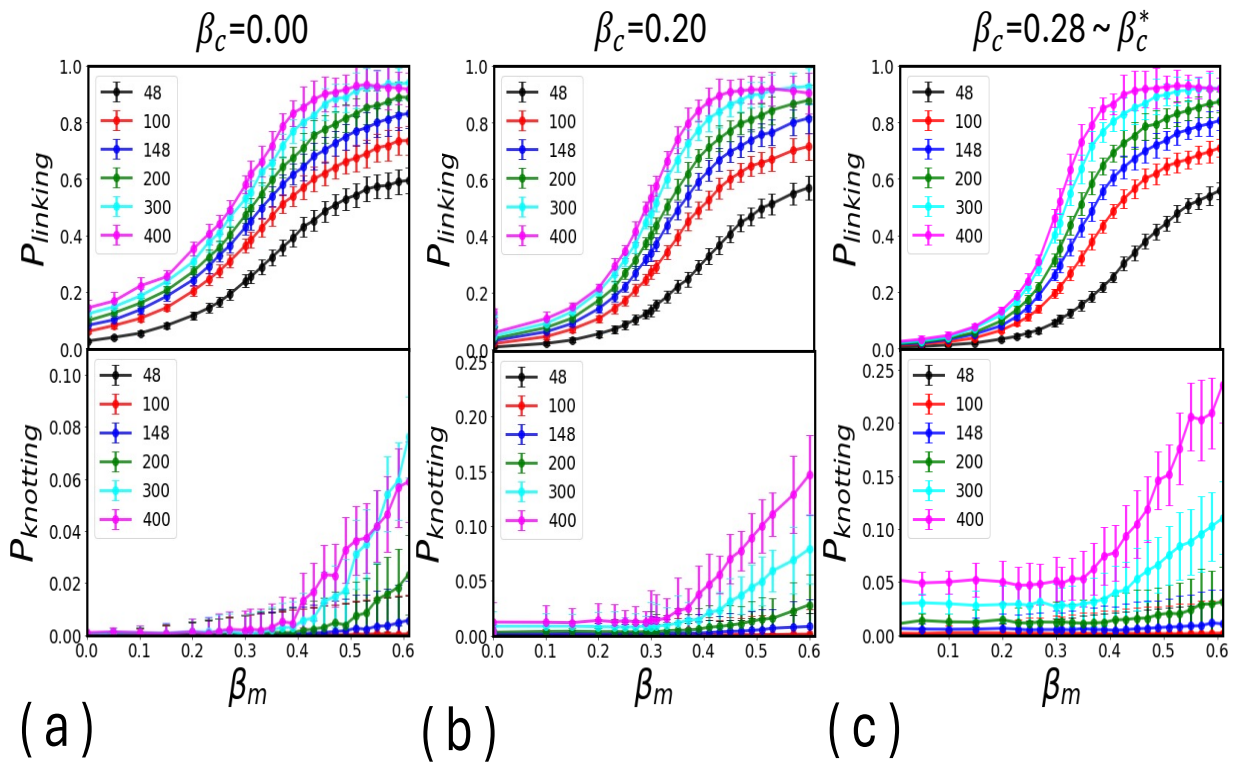

Figure 15: Topological entanglement as the SE-M phase boundary is crossed by varying β_m: Linking probability (top row) and knotting probability (bottom row) as a function of the mutual attraction parameter β_m for three fixed values of the self attraction parameter β_c, (a) 0.00, (b) 0.20 and (c) 0.28. Note that $\beta_c = 0.28$ is very close to the estimate of the θ-point β_c^0 (where the collapse transitionoccurs) when $\beta_m = 0$.

as the M-SC phase boundary is crossed in the collapsed phase, consistent with our observations above.

6.2 Fixing β_c and varying β_m

By fixing β_c and then increasing $\beta_m \in (0, 0.75)$ one can cross the SE-M phase boundary when β_c is small enough, or the SC-M phase boundary for β_c large enough (this is evident in the right panel of figure 4).

The probability of knotting and linking when the model crosses the SE-M phase boundary is shown in the top and bottom rows of panels in figure 15, respectively. Linking probabilities increase dramatically from near zero in the SE phase as the SE-M phase boundary is crossed. Knotting probability, on the other hand, increases mildly across this phase boundary. It is near zero in the SE phase, and shows a small, though significant, increase in the M phase.

For larger β_c (i.e., above the θ-point), the transition is from the SC phase to the M phase, and the β_m dependence of the linking and knotting probability is reported in figure 16. More specifically, the top row of panels shows that the linking probability (near zero in the SC phase) increases to very large values in the M phase with increasing β_m. Knotting probabilities, on the other hand,

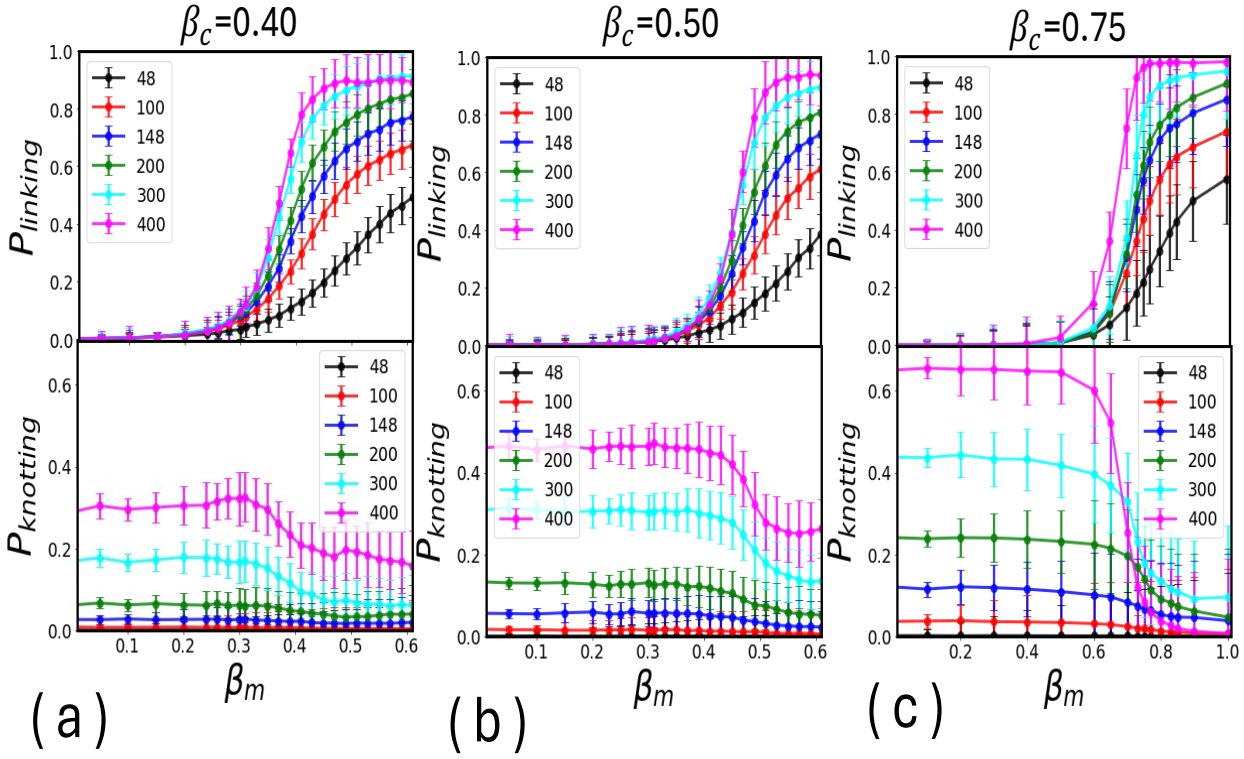

Figure 16: Topological entanglement as the SC-M phase boundary is crossed by varying β_m: Linking probability (top row) and knotting probability (bottom row) as a function of the mutual attraction parameter β_m for three fixed values of the self attraction parameter β_c, (a) 0.40, (b) 0.50 and (c) 0.758; all these values correspond to the system being well inside the collapse phase, at least for $\beta_m = 0$.

(see bottom row of panels) decrease as the SC-M phase boundary is crossed, from relatively large values in the SC phase, to smaller (but still significant) values in the M phase.

7 Discussion

In this paper we have constructed and analysed a lattice model of two ring polymers, close together in space. Each of the rings can collapse to a compact ball and, in addition, the rings can interpenetrate to form a mixed phase. The model contains two parameters: β_m controlling the extent of mixing, and a collapse parameter β_c. We have investigated the form of the phase diagram in the (β_c, β_m)-plane. We find evidence for three phases: A segregated-expanded (SE) phase, a segregated-compact (SC) phase, and a mixed (M) phase.

In section 2, we describe the model in more detail and make comments about the phase diagram. We provide some rigorous results in section 3, where we prove existence of a phase boundary between the segregated phases and the mixed phase. The two parts of this boundary are the SE-M and SC-M boundaries in figure 2. In addition we argue that the phase boundary between the SE and SC phases is a line at constant $\beta_c = \beta_c^0$.

In section 4, we give a brief description of the Monte Carlo method we use to investigate the phases in the phase diagram. We performed extensive simulations using a Multiple Markov Chain implementation [13, 14, 12] of the Metropolis Algorithm [15] on lattice polygons using pivot elementary moves [17] and local Verdier-Stockmayer style moves [16].

We discuss our results in sections 5 and 6. In section 5.1 we focus on thermodynamic properties of the model when the SE-SC phase boundary is crossed. In section 5.2 we give similar results when we cross the SE-M phase boundary. These transitions appear to be continuous. We examine the SC-M phase boundary in sections 5.3 and 5.4.

In section 6, we turn our attention to topological properties (knotting and linking) as the various phase boundaries are crossed.

Acknowledgement

EJJvR acknowledges financial support from NSERC Canada) in the form of Discovery Grant RGPIN-2019-06303. Maria Carla Tesi is a member of GNAMPA (Gruppo Nazionale per l' Analisi Matematica, la Probabilità e le loro Applicazioni) of INdAM (Istituto Nazionale di Alta Matematica).

References

[1] EJ Janse van Rensburg, E Orlandini, MC Tesi, and SG Whittington. Thermodynamic and topological properties of copolymer rings with a segregation/mixing transition. *J Phys A: Math Theor*, 55(43):435002, 2022.

[2] Y Ohta, Y Kushida, D Kawaguchi, Y Matsushita, and A Takano. Preparation, characterization, and nanophase-separated structure of catenated polystyrene- polyisoprene. *Macromolecules*, 41(11):3957–3961, 2008.

[3] P-F Cao, JD Mangadlao, A de Leon, Z Su, and RC Advincula. Catenated poly (ε-caprolactone) and poly (l-lactide) via ring-expansion strategy. *Macromol*, 48(12):3825–3833, 2015.

[4] Z Niu and HW Gibson. Polycatenanes. *Chem Rev*, 109(11):6024–6046, 2009.

[5] J Luengo-Márquez, S Assenza, and C Micheletti. Shape and size tunability of sheets of interlocked ring copolymers. *Soft Matter*, 20(33):6595–6607, 2024.

[6] D Sun and J Cho. Monte Carlo simulations on thermodynamic and conformational properties of catenated double-ring copolymers. *Phys Rev E*, 90(6):062601, 2014.

[7] L Tubiana, F Ferrari, and E Orlandini. Circular polycatenanes: Supramolecular structures with topologically tunable properties. *Phys Rev Lett*, 129(22):227801, 2022.

[8] MC Tesi, EJ Janse van Rensburg, Enzo Orlandini, DW Sumners, and SG Whittington. Knotting and supercoiling in circular DNA: A model incorporating the effect of added salt. *Physical Review E*, 49(1):868–872, 1994.

[9] E Orlandini and SG Whittington. Entangled polymers in condensed phases. *J Chem Phys*, 121(23):12094–12099, 2004.

[10] E Panagiotou, C Tzoumanekas, S Lambropoulou, K C Millett, and D N Theodorou. A study of the entanglement in systems with periodic boundary conditions. *Progr Theo Phys Supp*, 191:172–181, 2011.

[11] D Bennett-Wood, IG Enting, DS Gaunt, AJ Guttmann, JL Leask, AL Owczarek, and SG Whittington. Exact enumeration study of free energies of interacting polygons and walks in two dimensions. *J Phys A: Math Gen*, 31(20):4725–4741, 1998.

[12] MC Tesi, EJ Janse van Rensburg, E Orlandini, and SG Whittington. Interacting self-avoiding walks and polygons in three dimensions. *J Phys A: Math Gen*, 29(10):2451–2463, 1996.

[13] CJ Geyer and EA Thompson. Annealing Markov chain Monte Carlo with applications to ancestral inference. *J Amer Stat Ass*, 90(431):909–920, 1995.

[14] MC Tesi, EJ Janse van Rensburg, E Orlandini, and SG Whittington. Monte Carlo study of the interacting self-avoiding walk model in three dimensions. *J Stat Phys*, 82(1):155–181, 1996.

[15] N Metropolis, AW Rosenbluth, MN Rosenbluth, AH Teller, and E Teller. Equation of state calculations by fast computing machines. *J Chem Phys*, 21(6):1087–1092, 1953.

[16] PH Verdier and WH Stockmayer. Monte Carlo calculations on the dynamics of polymers in dilute solution. *J Chem Phys*, 36(1):227–235, 1962.

[17] N Madras, A Orlitsky, and LA Shepp. Monte Carlo generation of self-avoiding walks with fixed endpoints and fixed length. *J Stat Phys*, 58(1):159–183, 1990.

[18] H Kesten. On the number of self-avoiding walks. *J Math Phys*, 4:960–969, 1963.

[19] T Vrbová and SG Whittington. Adsorption and collapse of self-avoiding walks and polygons in three dimensions. *J Phys A: Math Gen*, 29:6253–6264, 1996.

[20] T Vrbová and SG Whittington. Adsorption and collapse of self-avoiding walks in three dimensions: a Monte Carlo study. *J Phys A: Math Gen*, 31:3989–3998, 1998.

[21] EJ Janse van Rensburg. Collapsing and adsorbing polygons. *J Phys A: Math Gen*, 31(41):8295–8306, 1998.

[22] GH Hardy, JE Littlewood, and G Pólya. *Inequalities*. Cambridge University Press, 1952.

[23] CJ Geyer. Markov chain Monte Carlo maximum likelihood. *Comp Sci and Stat: Proc 23rd Symp on the Interface*, pages 156–163, 1991.

[24] N Clisby. Accurate estimate of the critical exponent ν for self-avoiding walks via a fast implementation of the pivot algorithm. *Phys Rev Lett*, 104:055702, Feb 2010.

[25] JM Hammersley, GM Torrie, and SG Whittington. Self-avoiding walks interacting with a surface. *J Phys A: Math Gen*, 15:539–571, 1982.

[26] EJ Janse Van Rensburg. *The Statistical Mechanics of Interacting Walks, Polygons, Animals and Vesicles, 2ed*. Oxford University Press, 2015.

[27] G Torres. On the Alexander polynomial. *Ann Math*, 57(1):57–89, 1953.

[28] CH Dowker and MB Thistlethwaite. Classification of knot projections. *Top Appl*, 16(1):19–31, 1983.

[29] EJ Janse van Rensburg and SG Whittington. The knot probability in lattice polygons. *J Phys A: Math Gen*, 23(15):3573–3590, 1990.

[30] B Berg and D Foerster. Random paths and random surfaces on a digital computer. *Phys Lett B*, 106(4):323–326, 1981.

[31] C Aragao De Carvalho and S Caracciolo. A new Monte Carlo approach to the critical properties of self-avoiding random walks. *J de Physique*, 44(3):323–331, 1983.

[32] M Baiesi, E Orlandini, and AL Stella. Knotted globular ring polymers: How topology affects statistics and thermodynamics. *Macromol*, 47(23):8466–8476, 2014.

[33] KC Millett, EJ Rawdon, A Stasiak, and JI Sułkowska. Identifying knots in proteins. *Biochem Soc Trans*, 41(2):533–537, 2013.

[34] ML Mansfield. Development of knotting during the collapse transition of polymers. *J Chem Phys*, 127(24):244902, 2007.